

FULL PAPER

Open Access



# Recent geomagnetic secular variation from *Swarm* and ground observatories as estimated in the CHAOS-6 geomagnetic field model

Christopher C. Finlay<sup>1\*</sup> , Nils Olsen<sup>1</sup>, Stavros Kotsiaros<sup>1</sup>, Nicolas Gillet<sup>2</sup> and Lars Tøffner-Clausen<sup>1</sup>

## Abstract

We use more than 2 years of magnetic data from the *Swarm* mission, and monthly means from 160 ground observatories as available in March 2016, to update the CHAOS time-dependent geomagnetic field model. The new model, CHAOS-6, provides information on time variations of the core-generated part of the Earth's magnetic field between 1999.0 and 2016.5. We present details of the secular variation (SV) and secular acceleration (SA) from CHAOS-6 at Earth's surface and downward continued to the core surface. At Earth's surface, we find evidence for positive acceleration of the field intensity in 2015 over a broad area around longitude 90°E that is also seen at ground observatories such as Novosibirsk. At the core surface, we are able to map the SV up to at least degree 16. The radial field SA at the core surface in 2015 is found to be largest at low latitudes under the India–South-East Asia region, under the region of northern South America, and at high northern latitudes under Alaska and Siberia. Surprisingly, there is also evidence for significant SA in the central Pacific region, for example near Hawaii where radial field SA is observed on either side of a jerk in 2014. On the other hand, little SV or SA has occurred over the past 17 years in the southern polar region. Inverting for a quasi-geostrophic core flow that accounts for this SV, we obtain a prominent planetary-scale, anti-cyclonic, gyre centred on the Atlantic hemisphere. We also find oscillations of non-axisymmetric, azimuthal, jets at low latitudes, for example close to 40°W, that may be responsible for localized SA oscillations. In addition to scalar data from Ørsted, CHAMP, SAC-C and *Swarm*, and vector data from Ørsted, CHAMP and *Swarm*, CHAOS-6 benefits from the inclusion of along-track differences of scalar and vector field data from both CHAMP and the three *Swarm* satellites, as well as east–west differences between the lower pair of *Swarm* satellites, *Alpha* and *Charlie*. Moreover, ground observatory SV estimates are fit to a Huber-weighted rms level of 3.1 nT/year for the eastward components and 3.8 and 3.7 nT/year for the vertical and southward components. We also present an update of the CHAOS high-degree lithospheric field, making use of along-track differences of CHAMP scalar and vector field data to produce a new static field model that agrees well with the MF7 field model out to degree 110.

**Keywords:** Geomagnetism, Secular variation, Field modelling, Core dynamics, *Swarm*

## Introduction

The Earth's intrinsic magnetic field is gradually changing as a result of motional induction and Ohmic dissipation processes taking place within its metallic core. This

phenomenon, called geomagnetic secular variation (SV), has been well documented, but poorly understood, for centuries (e.g. Gellibrand 1635; Hansteen 1819). In 1980, MAGSAT provided the first truly global set of vector field observations. Combined with novel regularized inversion techniques, this enabled the structure of field at the core surface to be estimated for the first time with some confidence (Langel et al. 1980; Shure et al. 1982). Unfortunately, the MAGSAT mission lasted less than a year, so

\*Correspondence: cfinlay@space.dtu.dk

<sup>1</sup> Division of Geomagnetism, DTU Space, Technical University of Denmark, Diplomvej 371, Kongens Lyngby, Denmark

Full list of author information is available at the end of the article

inferences concerning SV were limited. It has only been in the past decade, thanks to the Ørsted and CHAMP missions, that it has become possible to map the large-scale patterns of the SV directly at the core surface (Lesur et al. 2008; Olsen et al. 2006). A picture has emerged of gradual (decadal) variations in SV punctuated by localized pulses of secular acceleration (SA) on shorter inter-annual timescales (Chulliat et al. 2010; Olsen et al. 2014). SA pulses provide an unexpected new window into the dynamics of the core, and we are still in the early stages of their study. We presently lack detailed knowledge of their morphology and their time dependence, and our understanding is severely limited by the relatively short time window for which there has been global monitoring from space.

A new opportunity for studying SV is today provided by the *Swarm* mission. Launched on 22 November 2013, it consists of three dedicated low-Earth-orbit satellites, each simultaneously measuring the near-Earth magnetic field. After more than 2 years of operation, *Swarm* data are starting to provide valuable new constraints on the time-varying SV. In this article, we present investigations of SV as observed by the *Swarm* satellites, and at ground observatories, in 2015 as part of a new time-dependent geomagnetic field model, called CHAOS-6, that also includes data from previous satellite missions (Ørsted, CHAMP, and SAC-C).

CHAOS-6 is the latest generation of the CHAOS series of global geomagnetic field models developed by Olsen et al. (2006, 2009, 2010, 2014). Ten months of *Swarm* data (up to September 2014) were included in the previous version, CHAOS-5 (Finlay et al. 2015), a model that was primarily designed for producing candidate field models for IGRF-12. With more than 2 years of *Swarm* data now available, given there have been advances in the use of spatial differences (gradients) in field modelling (Kotsiaros et al. 2014; Olsen et al. 2015), and because a geomagnetic jerk happened in 2014 (Torta et al. 2015), there is now a clear need to update the CHAOS model series and particularly its time-dependent part, as CHAOS-6.

The CHAOS model series aims to estimate the internal geomagnetic field at the Earth's surface with high resolution in space and time. It is derived primarily from magnetic satellite data, although ground-based activity indices and observatory monthly means are also used. It includes a parameterization of the quiet-time, near-Earth magnetospheric field, but there is no explicit representation of the ionospheric field or fields due to magnetosphere–ionosphere coupling currents. A limitation of the CHAOS models series is that its validity is restricted to after 1999, when the Ørsted satellite was launched.

Other models with continuous time dependence are available for studying core field variations on longer time-scales, although these typically have lower resolution in both space and time. The *gufm1* model (Jackson et al. 2000) is the definitive source for the historical field from 1590 to 1990. A more recent alternative spanning 1840 to 2010 is the COV-OBS model (Gillet et al. 2013) [see also Gillet et al. (2015a) for a version updated to 2015]. These models contain only a small amount of satellite data and are predominantly constrained by observatory data during the twentieth and twenty-first centuries. A rather different approach to modelling the recent field is provided by the comprehensive model series (Sabaka et al. 2004, 2015). The latest versions CM4 and CM5 cover 1960–2002 and 2000–2013, respectively, and involve simultaneous estimation of fields from a large number of sources including quiet-time ionospheric currents and magnetosphere–ionosphere coupling currents. This requires a much larger number of free parameters than is the case in the CHAOS models. A series of models of similar complexity to the CHAOS model, but derived only from CHAMP and ground observatory data, is the GRIMM series of models (Lesur et al. 2008, 2010, 2015). The latter study is particularly interesting because it proposed field models with time dependence controlled by co-estimated core flows.

The main purpose of this article is to present CHAOS-6, providing a reference for users regarding its construction. In the “Data” section, we detail the input data, while the model parameterization and estimation scheme are described in the “Field modelling” section. Model results and related discussion are presented in the “Results and discussion” section, including the fit to *Swarm* and CHAMP satellite data as well as ground observatory SV in the sections “Fit to satellite data” and “Fit to secular variation estimates from ground observatories”, respectively. The field and SV at Earth's surface are described in the sections “Power spectra of field, SV and SA at Earth's surface” and “Time changes in magnetic intensity at Earth's surface”. The lithospheric field part of CHAOS-6 is described in the section “CHAOS-6h and the high-degree lithospheric field”. The field, SV and SA at the core surface are described in the section “Secular variation and acceleration at Earth's core surface”. In the section “An interpretation based on quasi-geostrophic core flows”, we present for epoch 2015.0 a quasi-geostrophic flow derived from the CHAOS-6 time-dependent field and SV. A summary and perspectives are offered in the “Conclusions” section.

## Data

The database of magnetic observations used to construct CHAOS-6 is essentially an extension of that used by Finlay et al. (2015) to construct the CHAOS-5 model

in September 2014. The ground observatory vector field data have been updated as available in March 2016 (see the section “Ground observatory data”), while vector and scalar field data from the *Swarm* constellation up to 30 March 2016 have been included. The data selection criteria for satellite data at high latitudes have also been slightly altered compared with previous versions of the CHAOS model; further details are given in the “Satellite data” section.

A major improvement compared with CHAOS-5 is the inclusion of field spatial differences (i.e. approximate gradients) as data, along-track for both CHAMP and *Swarm Alpha, Bravo and Charlie*, and also east–west between *Swarm’s* lower satellite pair *Alpha* and *Charlie*. Along-track field differences approximate north–south gradients in non-polar regions (Kotsiaros et al. 2014; Sabaka et al. 2015), while the east–west differences provide information on the longitudinal gradient of the field (Olsen et al. 2015). We constructed along-track field differences from data points from the same satellite track, separated by 15 s. East–west difference data were found by searching *Swarm* L1b 1 Hz magnetic data for a datum from *Swarm Charlie*, with latitude closest to a selected *Swarm Alpha* datum, within a maximum time difference of 50 s. This procedure typically resulted in time shifts of about 10 s between the contributing *Alpha* and *Charlie* data.

**Ground observatory data**

Annual differences of revised observatory monthly means (Olsen et al. 2014) between January 1997 and December 2015 provide crucial constraints on the SV at fixed points on the Earth’s surface. Revised monthly means were derived from the hourly mean values of 160 observatories (for locations and IAGA codes see Fig. 1) that have been quality controlled, checking for trends, spikes and other errors (Macmillan and Olsen 2013). Quasi-definitive data (Peltier and Chulliat 2010; Clarke et al. 2013) were used when possible, for times when definitive data were not yet available; these quasi-definitive data are vital for determining up-to-date secular variation and for comparisons with the latest data from the *Swarm* mission. Starting from hourly mean values, estimates of the ionospheric (plus induced) field from the CM4 model (Sabaka et al. 2004) and the large-scale magnetospheric (plus induced) field from a preliminary CHAOS-type model, CHAOS-6pre, were subtracted. Then a Huber-weighted monthly mean, including all local times and all disturbance levels, is computed. Taking annual differences, this procedure resulted in 23,466 vector field triples of SV estimates.

**Satellite data**

The basic Ørsted, CHAMP and SAC-C dataset, sampled at a rate of 1 datum per 60 s, is the same as that employed in the earlier CHAOS-4 (Olsen et al. 2014) and

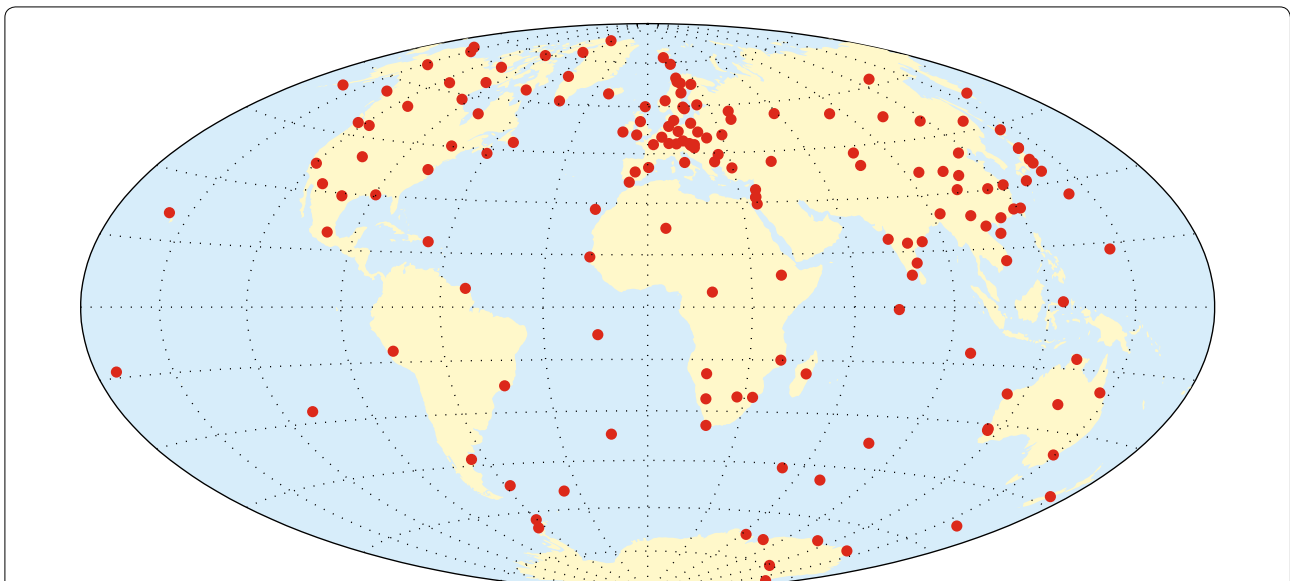


**Fig. 1** Locations of ground magnetic observatories whose data are used in the derivation of CHAOS-6. IAGA codes for the observatories are AAA, AAE, ABG, ABK, AIA, ALE, AMS, AMT, API, AQU, ARS, ASC, ASP, BDV, BEL, BFE, BFO, BGY, BJN, BLC, BMT, BNG, BOU, BOX, BRW, BSL, CBB, CBI, CDP, CKI, CLF, CMO, CNB, CSY, CTA, CZT, DLR, DLT, DMC, DOB, DRV, DVS, EBR, ELT, ESA, ESK, EYR, FCC, FRD, FRN, FUR, GAN, GDH, GLM, GNA, GNG, GUA, GUI, GZH, HAD, HBK, HER, HLP, HON, HRB, HRN, HTY, HUA, HYB, IPM, IQA, IRT, IZN, JCO, KAK, KDU, KEP, KHB, KIR, KIV, KMH, KNY, KNZ, KOU, KSH, KSH, LER, LIV, LMM, LNP, LOV, LRM, LRV, LVV, LYC, LZH, MAB, MAW, MBO, MCQ, MEA, MIZ, MMB, MOS, MZL, NAQ, NCK, NEW, NGK, NMP, NUR, NVS, OTT, PAF, PAG, PBQ, PET, PHU, PND, PST, QGZ, QIX, QSB, QZH, RES, SBA, SBL, SFS, SHU, SIL, SIT, SJG, SOD, SPT, SSH, STJ, SUA, TAM, TAN, TDC, TEO, TFS, THJ, THL, THY, TIR, TND, TRO, TRW, TSU, TUC, UPS, VAL, VIC, VSK, VSS, WHN, WIK, WNG, YAK, YKC

CHAOS-5 (Finlay et al. 2015) models. One difference compared with previous models is that CHAMP vector data were used only when attitude information from both star cameras was available.

Regarding the *Swarm* data, we used the *Swarm* Level-1b data product Mag-L, taking the latest available baseline 0408/09 data files in March 2016, for more than 28 months from 26 November 2013 to 30 March 2016. During this time, *Swarm Alpha* and *Charlie* descended from 514 to 445 km altitude, and *Swarm Bravo*, after being pushed up to 531 km altitude, has descended to 503 km. The local time of the ascending node of the three *Swarm* satellites has passed through more than two-and-a-half 24-hour cycles, and *Swarm Bravo* is now separated from *Swarm Alpha* and *Charlie* by about 3 h of local time. The nominal 1 Hz data were sub-sampled at 60-s intervals unless no vector field magnetometer (VFM) or star tracker (STR) data were available. In addition, we rejected known disturbed days (for example when satellite manoeuvres occurred) and excluded gross outliers for which the vector field components were more than 500 nT (and the scalar field more than 100 nT) from the predictions of a preliminary field model, CHAOS-6pre. In contrast to the case for CHAOS-5, no rescaling of *Swarm* vector data was necessary to ensure compatibility with the scalar data (Lesur et al. 2015), since the L1b baseline 0408/09 data calibration includes a co-estimated sun-driven disturbance that reduces rms scalar differences between the ASM and VFM measurements to under 200 pT (Tøffner-Clausen et al. 2016). After November 2014, calibration of the vector magnetometer on *Swarm Charlie* has been carried out using scalar field values mapped over from *Swarm Alpha*; this is necessary due to total failure of the absolute scalar magnetometers on *Swarm Charlie*.

Following experience with the *Swarm* Initial Field Model (SIFM, see Olsen et al. 2015) and in preliminary experiments for CHAOS-6, we use different selection criteria for different classes of data:

For vector field data, we adopt the same quiet-time, dark, selection criteria that were used for earlier versions of the CHAOS model series, namely (1) sun at least  $10^\circ$  below the horizon, (2) strength of the field due to the magnetospheric ring current, estimated using the RC index (Olsen et al. 2014), was required to change by at most 2 nT/h, (3) it was required that the geomagnetic activity index  $K_p \leq 2^0$  for quasi-dipole (Richmond 1995) latitudes equatorward of  $\pm 55^\circ$ .

As for earlier versions of the CHAOS model series, only scalar intensity data were used poleward of  $\pm 55^\circ$  quasi-dipole latitude, and these were selected only when the merging electric field at the magnetopause (averaged over the preceding hour)  $E_m \leq 0.8$  mV/m. In CHAOS-6,

$E_m$  was calculated using 1-min values of the interplanetary magnetic field (IMF) and solar wind speed from OMNIWeb (<http://omniweb.gsfc.nasa.gov>), in contrast to earlier versions of the CHAOS model where 5-min mean values were used. In addition, an additional selection criterion that IMF  $B_Z > 0$  was introduced in CHAOS-6, motivated by a desire to avoid as far as possible disturbances related to the sub-storm auroral electrojet that are especially prominent when IMF  $B_Z < 0$ . Scalar data were also used at lower latitudes when attitude data were not available.

In CHAOS-6, we also make use of along-track and east–west differences of scalar data. As for the *Swarm* Initial Field model, SIFM (Olsen et al. 2015), scalar field differences were used at all latitudes and for all local times (including sunlit conditions, but excluding day-side equatorial region  $< \pm 10^\circ$  quasi-dipole latitudes), with slightly relaxed quiet-time criteria (RC index required to change by at most 3 nT/h and  $K_p \leq 3^0$ ). The same selection criteria as for scalar data regarding  $E_m$  and IMF  $B_Z$  were applied to scalar field differences at polar latitudes. Scalar data have the advantage of not being directly perturbed by the field-aligned currents that are a major contribution to the unmodelled external fields, particularly at polar latitudes. Olsen et al. (2015) found that including spatial differences of scalar data helped to improve the quality of both lithospheric field and secular variation models.

Along-track differences of vector data from the single satellite mission CHAMP and both along-track and east–west vector differences from the *Swarm* mission were also employed. For the vector field differences, we used the same selection criteria as for the vector data itself i.e. only data from dark (sun at least  $10^\circ$  below the horizon), non-polar (equatorward of  $\pm 55^\circ$  quasi-dipole latitude) regions when the RC index changed by at most 2 nT/h and  $K_p \leq 2^0$  were selected.

For the low-degree part of CHAOS-6, called CHAOS-6l,  $3 \times 920,871$  vector data, 942,303 scalar data, 1,793,294 along-track scalar differences, 424,003 east–west scalar differences,  $3 \times 403,382$  along-track vector differences and  $3 \times 92,842$  east–west vector differences were used. The reason for the much larger number of scalar differences, compared with the number of scalar data, is that scalar differences were included for all local times (not just dark regions) and because their quiet-time selection criteria were less strict. As in previous versions of the CHAOS model, all satellite data were also weighted proportional to  $\sin \theta$ , where  $\theta$  is geographic co-latitude, in order to simulate an equal-area distribution.

Although iteratively reweighting of the data is performed during the model estimation (to implement a robust measure of misfit based on a Huber distribution of

errors, see the section “[Field modelling](#)”), we also employed an a priori error budget to account for the differences between the satellites. Regarding the scalar field, we assumed an a priori error estimate of 2.5 nT for Ørsted, CHAMP and SAC-C and 2.2 nT for *Swarm*. An isotropic pointing error estimate of 5 arc seconds was assumed for *Swarm*, 10 arc seconds for CHAMP (when both star cameras are available) and an anisotropic pointing error of 10 arc seconds and, respectively, 40 (60) arc seconds for after (before) 22 January 2000 for Ørsted. Note that these error estimates include the expected impact of unmodelled fields, which often dominate over instrumental errors.

## Field modelling

### Model parameterization

The model parameterization for CHAOS-6 follows closely that of CHAOS-5 and CHAOS-4. Since the focus of this article is the time-dependent internal field, we explicitly describe only this part of the model. See Olsen et al. (2014) for a more detailed account of the CHAOS field modelling scheme, including the external model. The time-dependent internal field  $\mathbf{B}^{\text{int}}(t) = -\nabla V^{\text{int}}(t)$  is represented as the gradient of the scalar potential

$$V^{\text{int}} = a \sum_{n=1}^{20} \sum_{m=0}^n [g_n^m(t) \cos m\phi + h_n^m(t) \sin m\phi] \times \left(\frac{a}{r}\right)^{n+1} P_n^m(\cos\theta) \quad (1)$$

where  $a = 6371.2$  km is a reference radius,  $(r, \theta, \phi)$  are geographic coordinates and  $P_n^m(\cos\theta)$  are the Schmidt semi-normalized associated Legendre functions of degree  $n$  and order  $m$ . Note that we follow the usual geomagnetic convention and refer to  $\mathbf{B}$  as the magnetic field, though it is strictly the magnetic flux density. In the vacuum, it is related to the magnetic field  $\mathbf{H}$  by  $\mathbf{B} = \mu_0\mathbf{H}$  where  $\mu_0$  is the permeability of free space.

$\{g_n^m(t), h_n^m(t)\}$  are time-dependent Gauss coefficients that are further expanded in a basis of sixth-order B-splines (De Boor 2001) such that

$$g_n^m(t) = \sum_{k=1}^K k g_n^m B_k(t), \quad (2)$$

and similarly for  $h_n^m(t)$ , where  $k g_n^m$  are the spline coefficients estimated for each Gauss coefficient,  $K = 6$  (sixth-order B-splines),  $B_k$  are the spline basis functions, and we use a 6-month knot spacing with fivefold repeated knots at the endpoints  $t = 1997.1$  and  $t = 2016.6$ .

In addition to a time-dependent internal field, we also estimate a static internal field above degree 20. The low-degree part of CHAOS-6 model that is the focus of this section, CHAOS-6l, was estimated using a maximum

degree of 80 (in contrast the high-degree part of the CHAOS-6 model, CHAOS-6h was estimated using a maximum degree of 120—see the section “[CHAOS-6h: estimation of the high-degree lithospheric field](#)”).

Regarding the external field, as in earlier CHAOS models, we use a representation of fields due to near-Earth magnetospheric sources, e.g. the magnetospheric ring current, in the *solar magnetic (SM)* coordinate system (up to  $n = 2$ , with time dependence for  $n = 1$  parameterized by the external and induced parts of the RC index) and of fields due to remote magnetospheric sources, e.g. magnetotail and magnetopause currents, in *geocentric solar magnetospheric (GSM)* coordinates (also up to  $n = 2$ , but restricted to order  $m = 0$ ). Additional offset parameters in bins of width 5 days, respectively, 30 days are included for the degree 1 SM terms, for orders  $m = 0$ , respectively  $m = 1$ .

We also co-estimate the Euler angles needed to describe the rotation between the vector magnetometer frame and the star imager frame. For Ørsted, this yields two sets of Euler angles (one for the period before 22 January 2000 when the onboard software of the star imager was updated and one for the period after that date), while for CHAMP and each *Swarm* satellite we solve for Euler angles in bins of 10 days.

### Model estimation

Model parameters were estimated using an *iteratively reweighted least-squares* algorithm making use of Huber weights. Regularization of temporal variations was also included. Specifically, we minimized the cost function

$$\mathbf{e}^T \underline{\underline{C}}^{-1} \mathbf{e} + \lambda_3 \mathbf{m}^T \underline{\underline{\Lambda}}_3 \mathbf{m} + \lambda_2 \mathbf{m}^T \underline{\underline{\Lambda}}_2 \mathbf{m} \quad (3)$$

where  $\mathbf{m}$  is the model vector,  $\underline{\underline{C}}$  is the data error covariance matrix which includes anisotropic errors due to attitude uncertainty (Holme and Bloxham 1996) and  $\underline{\underline{\Lambda}}_3$  and  $\underline{\underline{\Lambda}}_2$  are block diagonal regularization matrices penalizing the squared values of the third, respectively second, time derivatives of the radial field  $B_r$  at the core surface.  $\underline{\underline{\Lambda}}_3$  involves integration over the full time span of the model, while  $\underline{\underline{\Lambda}}_2$  involves evaluating the second time derivative only at the model endpoints  $t = 1997.1$  and  $2016.6$ .  $\lambda_3$  and  $\lambda_2$  determine the strength of the regularization applied to the model time dependence during the entire modelled interval and at the endpoints, respectively. We tested several values for these parameters and finally selected  $\lambda_3 = 0.66 (\text{nT/year}^3)^{-2}$ ,  $\lambda_2 = 100 (\text{nT/year}^2)^{-2}$  for the start time  $t = 1997.1$  and  $\lambda_2 = 300 (\text{nT/year}^2)^{-2}$  for the end time  $t = 2016.6$ . All time-dependent zonal terms were treated separately with  $\lambda_3$  set to a larger value of  $60 (\text{nT/year}^3)^{-2}$ .

The vector of residuals  $\mathbf{e}$  comprises differences between data and model predictions

$$\mathbf{e} = \begin{bmatrix} \mathbf{d}_{\text{obs}} \\ \Delta \mathbf{d}_{\text{obs}} \end{bmatrix} - \begin{bmatrix} \mathbf{d}_{\text{mod}} \\ \Delta \mathbf{d}_{\text{mod}} \end{bmatrix}. \quad (4)$$

It involves vector and scalar data, denoted by  $\mathbf{d}_{\text{obs}}$ , and the associated model predictions  $\mathbf{d}_{\text{mod}} = \mathbf{G}\mathbf{m}$ , where  $\mathbf{G}$  is the design matrix for the forward model. For scalar data,  $\mathbf{G}$  is the forward operator linearized around the present model. The data in CHAOS-6 also include along-track and east–west vector and scalar field differences, denoted by  $\Delta \mathbf{d}_{\text{obs}} = \mathbf{d}_{\text{obs}}(\mathbf{r}_2, t_2) - \mathbf{d}_{\text{obs}}(\mathbf{r}_1, t_1)$ . The associated model predictions are  $\Delta \mathbf{d}_{\text{mod}} = \Delta \mathbf{G}\mathbf{m} = [\mathbf{G}(\mathbf{r}_2, t_2) - \mathbf{G}(\mathbf{r}_1, t_1)]\mathbf{m}$ . Further details of the implementation of along-track and across-track differences in field modelling are described by Kotiaros et al. (2014) and Olsen et al. (2015, 2016).

In deriving the CHAOS-6l time-dependent field model, we estimated 28,766 model parameters from 7,481,013 observations. The final model was obtained after 9 iterations.

#### CHAOS-6h: estimation of the high-degree lithospheric field

The final version of CHAOS-6 was obtained by taking the model coefficients from CHAOS-6l (as described above) and replacing the static field Gauss coefficients above degree  $n = 24$  with the static field coefficients from the CHAOS-6h model, truncated at degree  $n = 110$ . CHAOS-6h is a new dedicated model of the high-degree lithospheric field. As for the CHAOS-4h model (Olsen et al. 2014), that provided the high-degree static field in both CHAOS-4 and CHAOS-5, it was derived only using low-altitude, solar minimum CHAMP data, from August 2008 to September 2010.

In addition to scalar and vector field data, CHAOS-6h makes use of along-track scalar and vector field differences from CHAMP. The data selection criteria for the vector and scalar field data are the same as for CHAOS-6l. However, for CHAOS-6h, identical selection criteria are used for both scalar and vector field differences. Data are selected only if  $K_p \leq 3^0$ , and  $|dD_{st}/dt| \leq 3$  nT/h. Both night and dayside data are selected, excluding the dayside equatorial region ( $< \pm 10^\circ$  quasi-dipole latitudes). Regarding the CHAOS-6h model parameterization, a static field up to  $n = 120$  was estimated, with a time-dependent internal field for  $n \leq 16$  described by a third-order Taylor expansion (quadratic SV). The same bin lengths as in CHAOS-6l were used for the RC baseline correction terms and for the instrument alignment calibration parameters (Euler angles). As for CHAOS-4h (Olsen et al. 2014), we applied regularization above degree  $n = 90$  by minimizing the L2 norm of  $B_r$  at Earth's surface.

In all, 15,636 model parameters were estimated from 3,306,074 CHAMP observations when deriving CHAOS-6h.

## Results and discussion

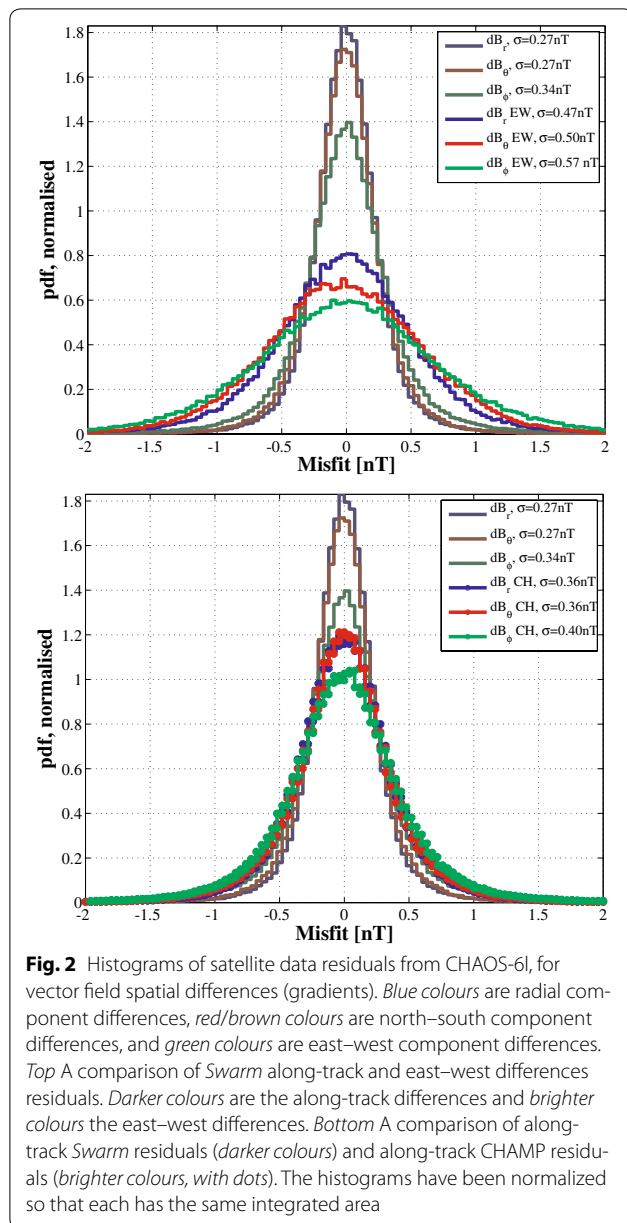
### Fit to satellite data

The fit of the CHAOS-6l field model to scalar and vector satellite data is generally similar (within 0.15 nT) to the fits achieved by CHAOS-5. For example, the Huber-weighted rms misfit between CHAOS-6l and non-polar scalar field data is 2.12 nT for CHAMP in comparison with 2.20 nT, 2.18 nT and 2.19 nT, respectively, for *Swarm Alpha*, *Beta* and *Charlie*. The misfit to the  $B_\phi$  vector component is 2.54 nT for CHAMP and 2.50, 2.47 and 2.50 nT, respectively, for *Swarm Alpha*, *Beta* and *Charlie*.

Field difference data were not included in earlier CHAOS models; CHAOS-6 is the first field model to be derived using along-track spatial differences of vector data from both CHAMP and *Swarm*. Figure 2 presents histograms of residuals for the vector field differences. Comparing *Swarm* along-track and east–west differences, the along-track differences (involving measurements made on the same orbit by the same instrument) have Huber-weighted rms misfits of 0.27, 0.27 and 0.34 nT for the radial, north–south and east–west components, compared with 0.47, 0.50 and 0.57 nT for the east–west vector field differences between *Swarm Alpha* and *Charlie*. Despite involving measurements from different satellites, we conclude the east–west vector field differences from *Swarm* are reliable and an internal field model is able to fit them to a weighted rms level of approximately 0.5 nT. Of course no east–west differences were possible with CHAMP, but we can compare the along-track differences. We find Huber-weighted rms misfits of 0.36, 0.36 and 0.40 nT for along-track differences of the radial, north–south and east–west vector field components from CHAMP. The along-track differences of *Swarm* vector data thus have generally smaller residuals than similar differences constructed with CHAMP data. This augurs well for the future of the *Swarm* mission as the satellites descend.

### Fit to secular variation estimates from ground observatories

The highest quality records of geomagnetic secular variation and its time variability come from ground magnetic observatories, where absolute calibrations are routinely carried out. If we are to use CHAOS-6 (which is primarily determined by fitting satellite data) to study secular variation, it is essential that it also fits the available ground observatory data well. We find Huber-weighted rms misfits of CHAOS-6 to annual differences of ground observatory revised monthly means of 3.80, 3.65 and 3.07



nT/year, respectively, for the radial, north–south and east–west components.

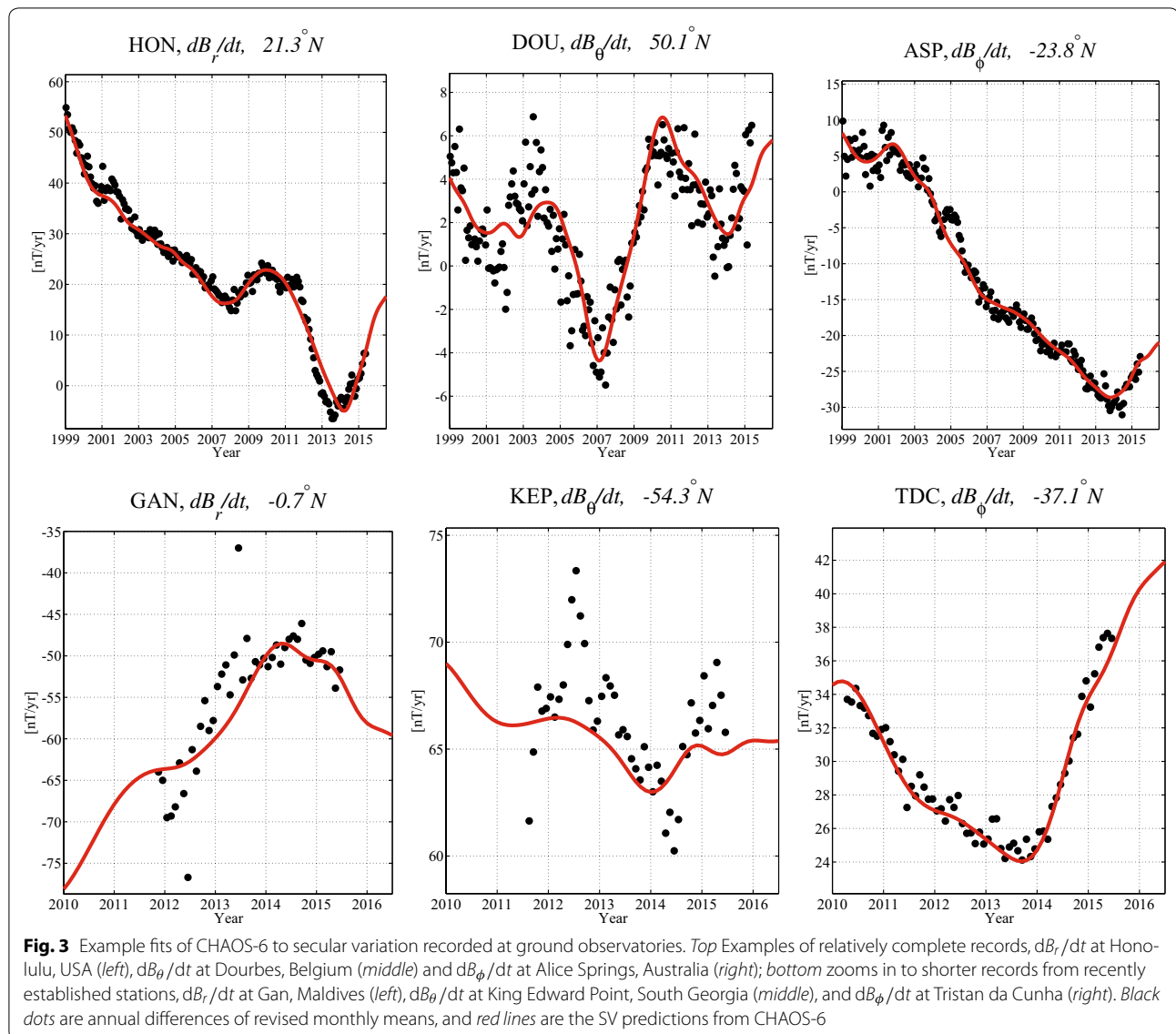
Examples of ground observatory secular variation time series, along with CHAOS-6 model predictions, are presented in Fig. 3. The top row shows examples of some complete series spanning 1999 to 2016 from well-established observatories at Honolulu (HON) in the central Pacific, at Dorbes (DOU) in Europe and at Alice Springs (ASP) in Australia. We find that CHAOS-6 provides a good description of the time-dependent SV in all these locations. There are noticeable sub-decadal changes in the SV trends even in the central Pacific where SV is often considered to be less intense. As pointed out by

Torta et al. (2015), a geomagnetic jerk (characterized by a ‘V’ shape in the SV as the SA changes sign) clearly occurred in 2014. This jerk event is generally well captured by the CHAOS-6 model.

In addition to presenting examples from well-established observatories, Fig. 3 also shows shorter time series at three recently established observatories in remote locations, at Gan in the southern Maldives, at King Edward Point (KEP) in South Georgia and at Tristan da Cunha (TDC) in the mid-Atlantic. Note that these plots are zoomed in compared to the previous plots and they cover only the shorter time interval of 2010–2015. CHAOS-6 again satisfactorily fits the data from these newer observatories, even when sharp changes in SV are observed, for example in  $dB_\phi/dt$  at Tristan da Cunha in 2014. Although the fit to KEP in Fig. 3 is visually less impressive than that at TDC, note that it is for the north–south field component, while the (typically quieter) east–west component is presented for TDC. The rms weighted residuals for  $dB_r/dt$ ,  $dB_\theta/dt$ ,  $dB_\phi/dt$  are, respectively, 1.2, 1.6, 0.9 nT/year for TDC and 1.65, 2.40, 2.09 nT/year for KEP.

#### Power spectra of field, SV and SA at Earth’s surface

In Fig. 4, we present the Lowes–Mauersberger spherical harmonic power spectra for the vector field, its first time derivative (SV) and its second time derivative (SA) at the Earth’s surface in 2015. The spectra for the field itself decreases steadily until approximately degree 14, after which it begins to level out. The change from a negative (decreasing) slope to a positive (increasing) slope, which indicates that lithospheric sources are certainly dominating, does not take place until degree 18. At the Earth’s surface, the spectrum of the SV also decreases with degree; the slope begins to level out about degree 19, indicative of the noise floor being reached. In contrast to the field and the SV, the SA spectra converges at the surface for CHAOS-6 in 2015, with essentially zero power remaining by its truncation degree 20. This is a consequence of the model regularization, that forces the SA towards zero at the model endpoints and minimizes time changes in the SA throughout, which is stronger at higher degree. The low values of the SA spectrum at high degrees should thus not be taken as indicative of a detection limit for the SA which would be related to the noise spectrum; the detection limit can only be properly assessed in unregularized inversions. The SA power spectrum shows weak peaks at degrees 3, 5, 7 and 9 in 2015. Given the surface spectra are well behaved and not diverging, the entire time-dependent part of the CHAOS-6 model (up to spherical harmonic degree 20) can legitimately be used to map and investigate time-dependent secular variation at the Earth’s surface.



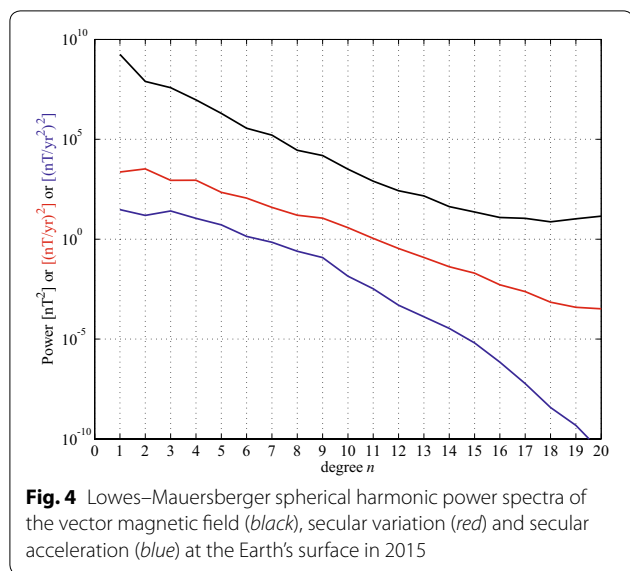
### Time changes in magnetic intensity at Earth's surface

It is well known that the magnetic field intensity  $F$  at Earth's surface is changing, with the South Atlantic Anomaly growing in size and moving westwards. With CHAOS-6, it is possible to map both trends and accelerations in the field intensity at Earth's surface. In Fig. 5, we present maps of  $F$ ,  $dF/dt$  and  $d^2F/dt^2$  at Earth's surface in 2015. We calculate  $dF/dt$  in 2015 from  $F$  in 2015.5 minus  $F$  in 2014.5 and similarly  $d^2F/dt^2$  in 2015 from  $dF/dt$  in 2015.5 minus  $dF/dt$  in 2014.5.

We find that the field is presently strengthening in general in the eastern hemisphere and weakening in the western hemisphere. This is partly a consequence of the low-intensity South Atlantic Anomaly moving to the west, bringing lower field strengths with it, while stronger

fields replace it in the east as it moves away. But in addition between 1999 and 2016 the maxima of field intensity over North America have clearly decreased in amplitude, while the field intensity maxima over Northern Asia has grown. A movie of the evolution of  $F$  is available at [www.spacecenter.dk/files/magnetic-models/CHAOS-6](http://www.spacecenter.dk/files/magnetic-models/CHAOS-6).

Examining the acceleration of the intensity ( $d^2F/dt^2$ ), we find a strong positive acceleration is now taking place in the east, in a broad longitudinal sector from 30° to 120°E. There is also a notable patch of negative acceleration in field intensity around South-West Africa and a negative acceleration taking place close to Alaska and in the northern Pacific region. Considering a time series of such field intensity acceleration maps from 2000 to 2015 (also available as a movie at [www.spacecenter.dk/](http://www.spacecenter.dk/)

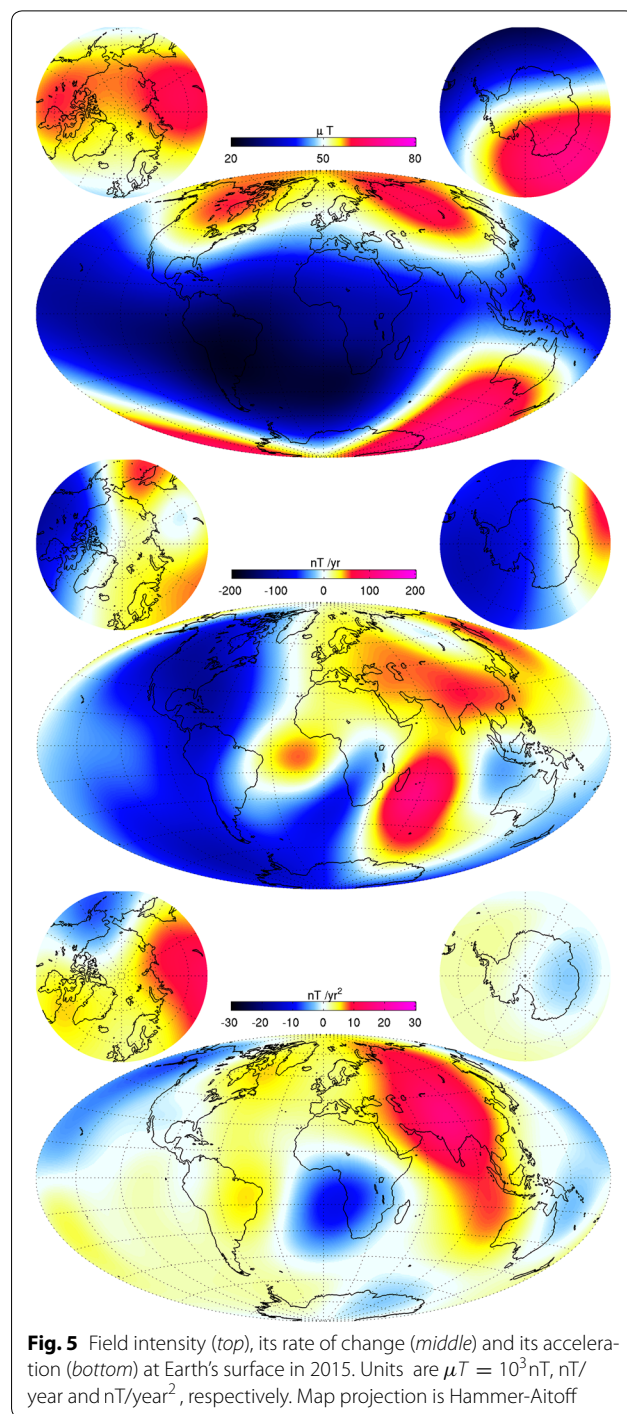


files/magnetic-models/CHAOS-6), we find the intensity acceleration changes dramatically on sub-decadal time-scales. For example, a series of prominent oscillations are observed west of southern Africa. The field, the SV and the SA downward continued to the core surface are presented later in the section “Secular variation and acceleration at Earth’s core surface” and in Fig. 9.

In order to test the above inferences concerning field intensity changes made using the CHAOS-6 field model, in Fig. 6 we present time series of field intensity changes, based on annual differences of ground observatory revised monthly means ( $F$  is in this case calculated from the revised month values of  $B_r, B_\theta, B_\phi$ ). A positive intensity acceleration in 2015 is clearly seen at Novosibirsk, Russia, at eastern longitudes in the northern hemisphere and is also evident although weaker at Niemegek, Germany, and at Learmouth, Australia. A relatively long-term negative acceleration is evident in the rate of field intensity decrease observed in Alaska. Overall, we are satisfied that CHAOS-6 adequately explains the observed trends and accelerations of the recent geomagnetic field intensity.

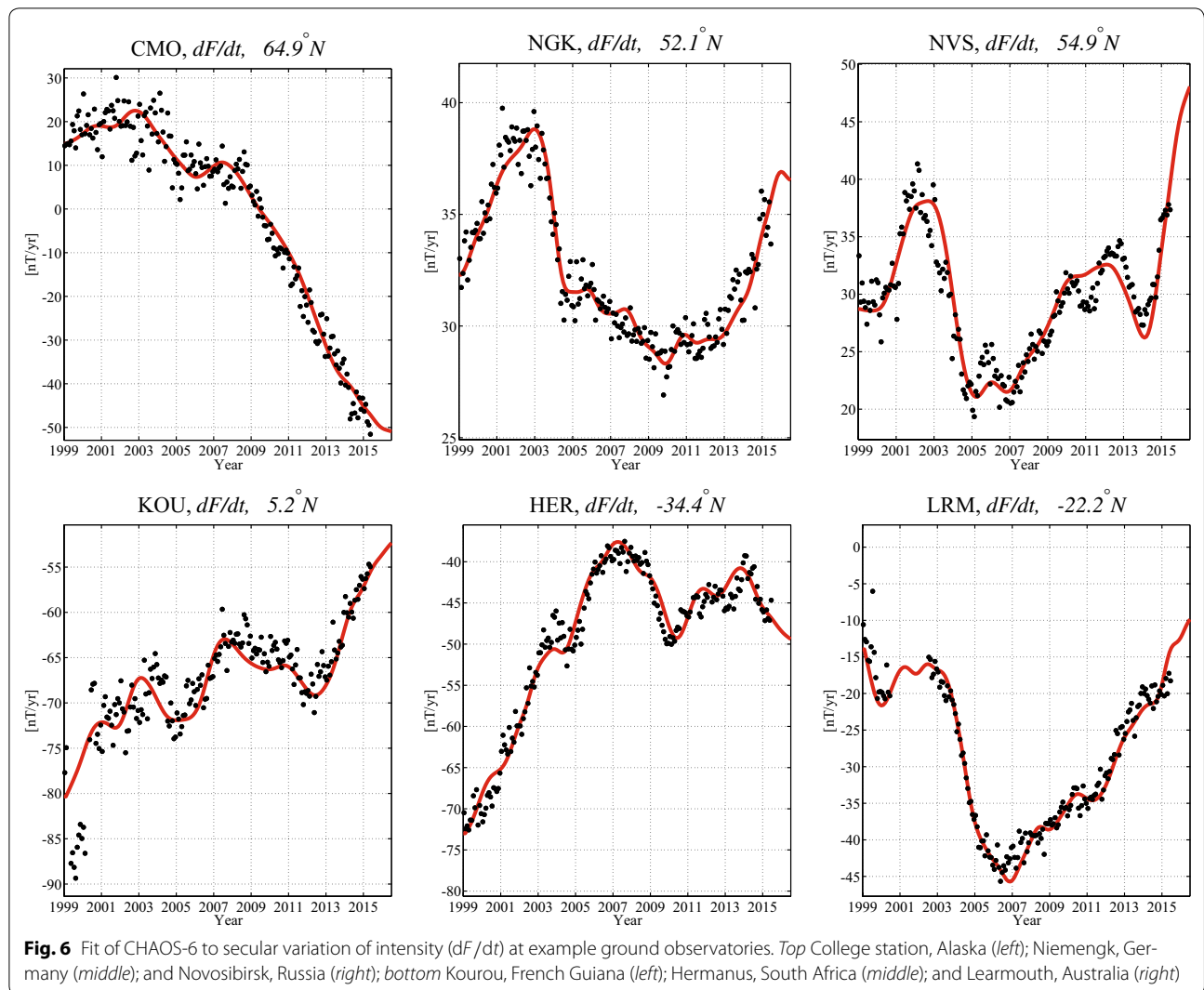
**CHAOS-6h and the high-degree lithospheric field**

Turning to the higher degree static field in CHAOS-6 (from CHAOS-6h, see the section “CHAOS-6h: estimation of the high-degree lithospheric field”), Fig. 7 presents a map of the lithospheric part of the radial field (degrees 15–110) along with the power spectrum and degree correlation at the Earth’s surface in comparison with MF7 (Maus 2010) and CHAOS-4. CHAOS-6 agrees with MF7 much better than CHAOS-4 whose power spectra begin to show deviations above degree 83, when the degree correlation also drops below 0.85. In contrast, the spectrum



for CHAOS-6 remains close to that of MF7 up to degree 110, and only after this, does its degree correlation fall below 0.85. We therefore consider the static field in CHAOS-6 to be reliable up degree 110 and recommend its use to this degree.

The map in Fig. 7 shows the radial field plotted at the Earth’s surface considering degrees 16 to 110. The map



displays well-localized anomalies, especially over the continents. Over the oceans, short-wavelength north-south linear features are visible, despite their relatively low amplitude. Differences to MF7 are mostly with respect to these features. Some differences, especially around auroral electrojet latitudes south of Australia, are possibly due to disturbed tracks, but it may also be that MF7 lacks some along-track power due to the filtering applied during its construction. It will be interesting to see how this part of the signal develops in future models constructed from *Swarm* data, as the lower pair of satellites descend and they are better able to resolve the short-wavelength east-west field gradients.

Statistics regarding the Huber-weighted mean and rms misfits of CHAOS-6h to the CHAMP field and field difference data used to construct it are presented in Table 1.

### Secular variation and acceleration at Earth's core surface

In order to study the origin of secular variation, it is necessary to downward continue the field to the outer edge of its source region in the core. We carry out the downward continuation, assuming that there are no current sources in the mantle on the timescale of observable secular variation, so the field continues to be described by a potential. The resulting spectra for the field, SV and SA at the core surface in 2015 are presented in Fig. 8.

Above degree 13, we see an upward trend in the field spectrum that we attribute to lithospheric sources. We therefore choose to present maps of the field at the core surface only to degree 13. The SV spectra increases rapidly with degree at first, but levels out above degree 9. It starts to increase more rapidly again above degree 18; plotting maps of the SV at the core surface, we see this

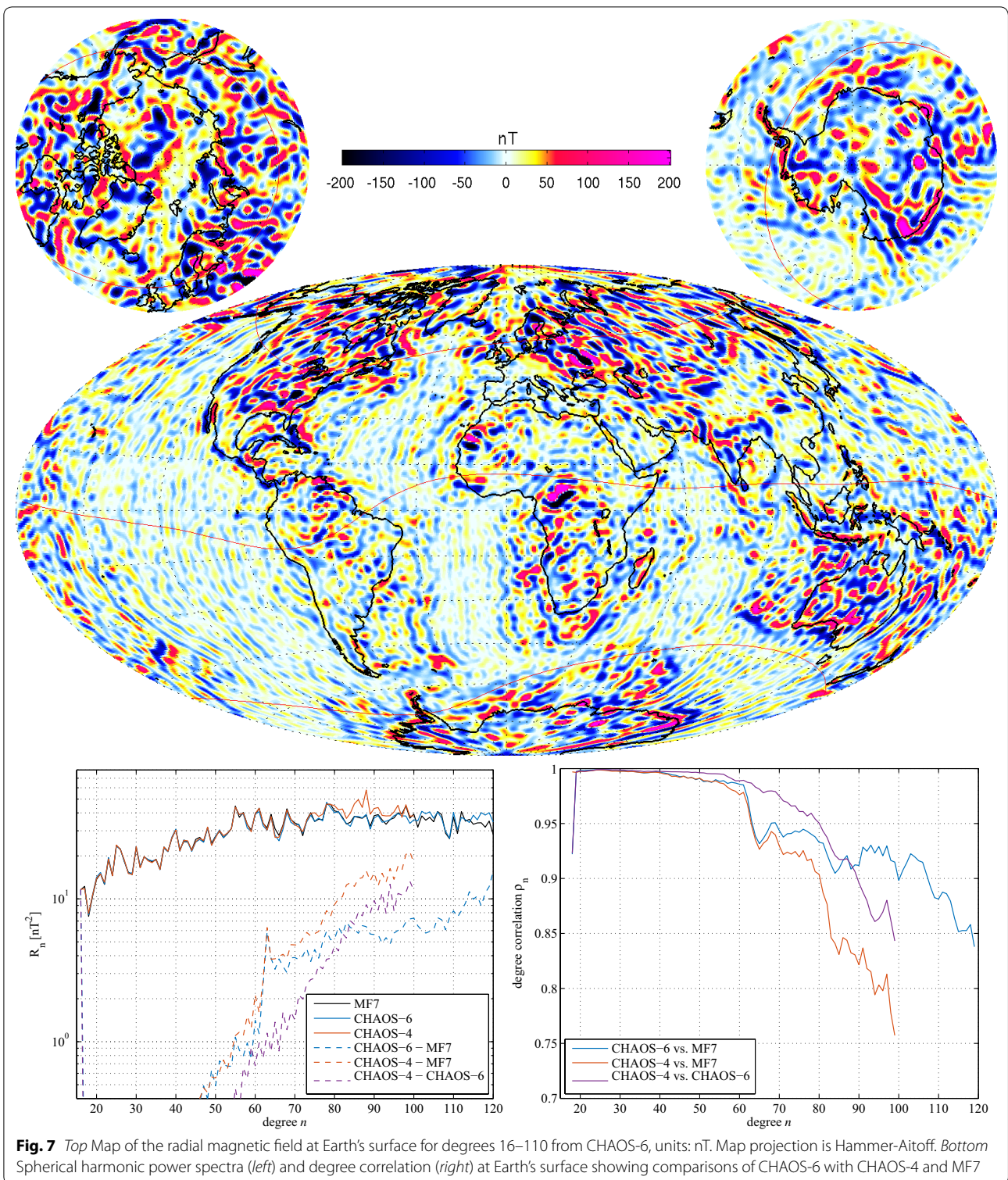


**Fig. 7** Top Map of the radial magnetic field at Earth's surface for degrees 16–110 from CHAOS-6, units: nT. Map projection is Hammer-Aitoff. Bottom Spherical harmonic power spectra (left) and degree correlation (right) at Earth's surface showing comparisons of CHAOS-6 with CHAOS-4 and MF7

is associated with an increase in disorganized noise in maps. We therefore believe the SV in CHAOS-6 is satisfactory out at least to degree 16, and possibly even as far as degree 18. Turning to the SA spectrum, in CHAOS-6

this converges at high degree at the core surface due to the applied regularization. In 2015 (relatively close to the model endpoint), regularization starts to dominate the solution already above degree 9. We nonetheless choose

**Table 1** CHAOS-6h model misfit statistics

|                     | Component                 | N       | Mean (nT) | rms (nT) |
|---------------------|---------------------------|---------|-----------|----------|
| Field               | $F_{\text{polar}}$        | 116,437 | -0.01     | 4.10     |
|                     | $B_r$                     | 295,780 | -0.03     | 1.77     |
|                     | $B_\theta$                |         | 0.01      | 2.63     |
|                     | $B_\phi$                  |         | -0.06     | 2.09     |
| Differences         | $\Delta F_{\text{polar}}$ | 696,807 | -0.01     | 1.47     |
| Differences, dark   | $\Delta B_r$              | 397,656 | 0.00      | 0.33     |
|                     | $\Delta B_\theta$         |         | 0.00      | 0.36     |
|                     | $\Delta B_\phi$           |         | 0.00      | 0.39     |
| Differences, sunlit | $\Delta B_r$              | 137,507 | -0.02     | 0.82     |
|                     | $\Delta B_\theta$         |         | -0.01     | 0.99     |
|                     | $\Delta B_\phi$           |         | 0.00      | 1.04     |

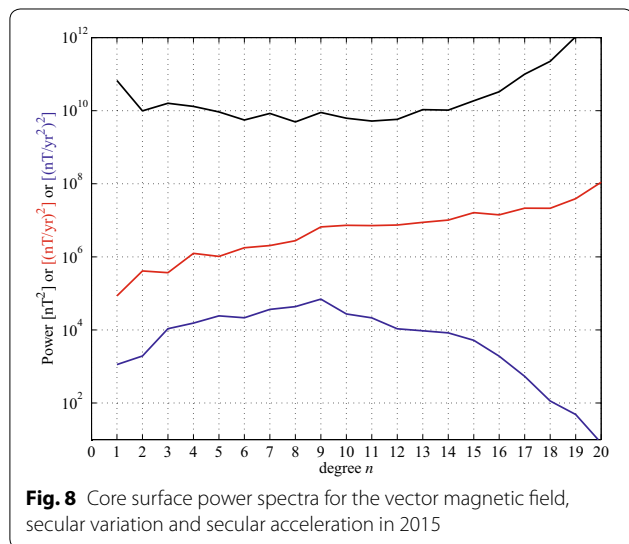


**Fig. 8** Core surface power spectra for the vector magnetic field, secular variation and secular acceleration in 2015

to present the SA at the core surface also to degree 16, since some information on rapid field changes is possible up to this degree, particularly for epochs more distant from the model endpoints. Maps of the radial field to degree 13 as well as radial SV and radial SA to degree 16 at the core surface in 2015 are presented in Fig. 9. Movies showing the time changes of such maps are available at [www.spacecenter.dk/files/magnetic-models/CHAOS-6](http://www.spacecenter.dk/files/magnetic-models/CHAOS-6).

We find that regions of intense radial SV at the core surface occur close to edges of patches of strong radial field that can be seen to drift when examining a sequence of maps (or a movie) of the radial field between 1999 and 2016. Intense SV in 2015 is observed to lie in a broad band equatorward of 30° latitude between longitudes 100°E and 90°W. There is also a well-localized

negative–positive–negative series of three patches of radial SV visible under Alaska and Siberia; this appears to be a consequence of a very rapid westward movement of the intense high-latitude radial field patches. The SV is also generally large in the longitudinal sector from 60° to 120°E, particularly in the northern hemisphere.

Regarding the radial field SA at the core surface in 2015, the most prominent features are a positive–negative pair under India–South-East Asia, a series of strong radial SA patches of alternating sign in the region under northern South America, and a positive–negative pair at high northern latitudes under Alaska–Siberia, that is linked to the evolution of the high-latitude SV patches described above.

In both the radial SV and SA, there is a striking absence of structure in the southern polar region (see also the discussion in Holme et al. 2011; Olsen et al. 2014). Although the Pacific region shows lower amplitude radial SV (again see Holme et al. 2011; Olsen et al. 2014), we note that in 2015 there is strong radial SA in the central Pacific, consistent with the aftermath of the jerk observed in 2014 at Hawaii (see Fig. 3, top left). Although the flows driving SV may be weaker in this region, they nonetheless seem to undergo similar time variations.

Earlier versions of the CHAOS model (Finlay et al. 2015) as well as independent models based on CHAMP and DMSP data (Chulliat and Maus 2014; Chulliat et al. 2015) have demonstrated that the SA undergoes dramatic changes on sub-decadal timescales, notably exhibiting a series of pulses in amplitude. In Fig. 10, power spectra of the SA at the core surface for a number of epochs, and the L2 norm of the SA at the core surface (e.g. Finlay et al. 2015), calculated for different spherical harmonic truncation levels, are presented for CHAOS-6. The applied regularization forces the SA spectra to decay at high degree and it begins to have an influence already between degree 10 and 12, especially close to the model endpoints. We find peaks in the SA norm, indicating pulses of SA, for all the investigated truncation levels, at around 2006, 2009.5 and 2013. The exact time of the pulses depends on the chosen truncation level of the SA, which was usually set to degree 6, 8 or 9 in earlier studies. The relative sizes of the pulses also change with the chosen truncation level. As is also evident from the associated power spectra, the 2006 pulse displayed more power at high degrees (10–15), while the 2013 pulse has relatively more power at lower odd degrees 5, 7, 9. Although each pulse has a different spectral signature, there is always enhanced power in the band of degrees from 5 to 7. Maps and movies of the radial SA at the core surface also show recurring oscillations at particular

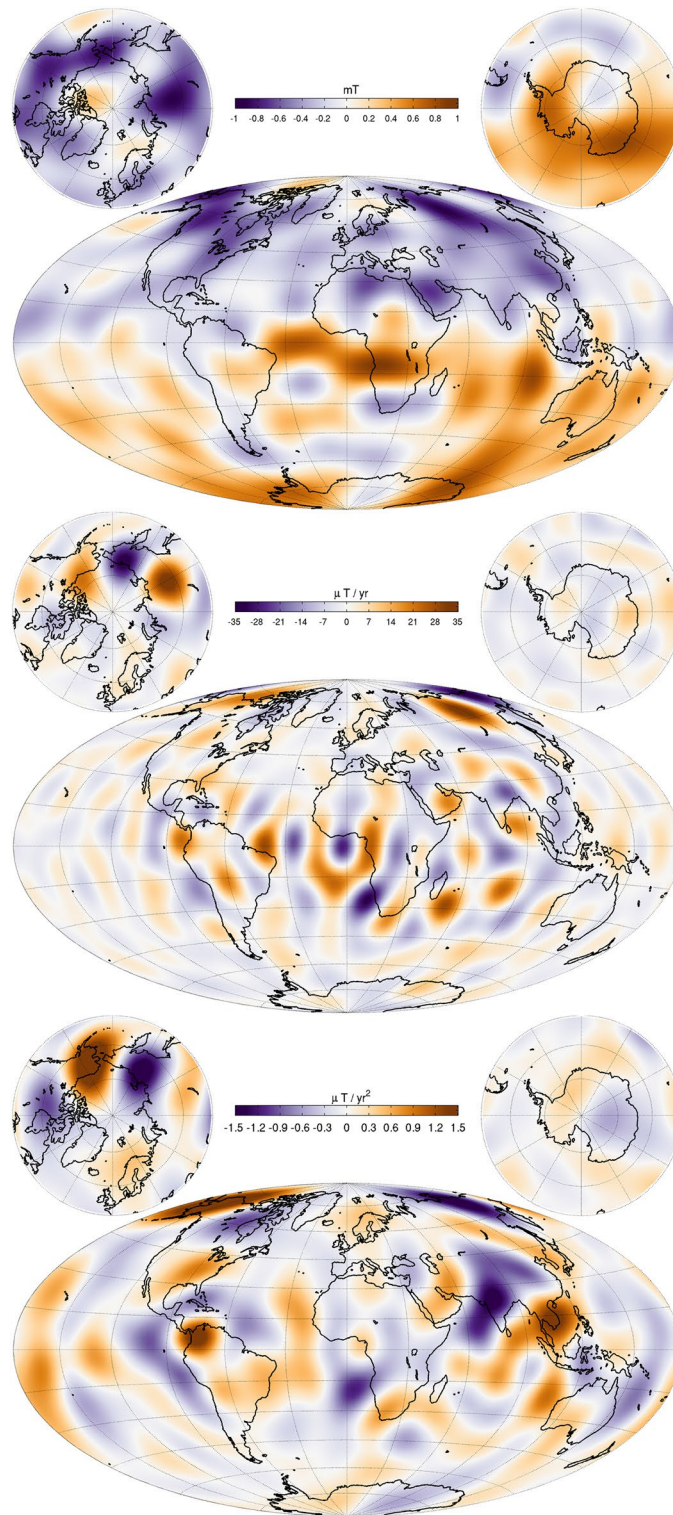
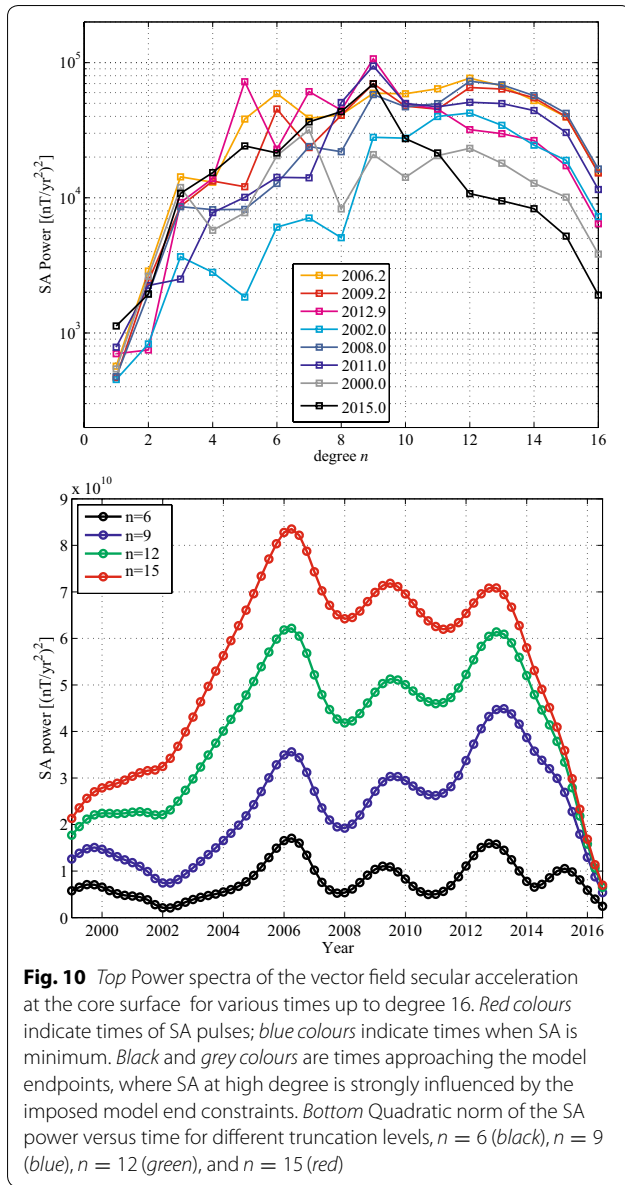


**Fig. 9** Radial field to degree 13, radial secular variation (SV) and radial secular acceleration (SA), both to degree 16, at the core surface in 2015. Units are  $\text{mT} = 10^6 \text{nT}$ ,  $\mu\text{T}/\text{year} = 10^3 \text{nT}/\text{year}$  and  $\mu\text{T}/\text{year}^2 = 10^3 \text{nT}/\text{year}^2$ . Map projection is Hammer-Aitoff



locations, for example under northern South America around  $40^\circ\text{W}$  close to the equator. High-amplitude SA is often present around longitude  $100^\circ\text{E}$ .

Present limitations in our ability to infer the high-degree SA in 2015 are also illustrated in Fig. 10. The power spectra of the SA in 2015 drops rapidly above spherical harmonic degree 9. Looking at the SA norm versus time, we see that this is a consequence of the imposed model end constraints which force the SA towards zero in 2016. The end constraints have less influence on the lower degrees (for example, see the SA norm truncated at  $n = 6$ ), but a longer time span of data is certainly required in order to better determine the high-degree ( $n > 9$ ) SA in 2015.

### An interpretation based on quasi-geostrophic core flows

One possible interpretation of the observed secular variation is in terms of rotation-dominated (or quasi-geostrophic) flows of liquid metal in the outer core. An estimate of the responsible flow may be obtained by inverting the magnetic induction equation evaluated at the surface of the core,

$$\frac{\partial B_r}{\partial t} = -\nabla_H \cdot (\mathbf{u} B_r), \quad (5)$$

where  $\mathbf{u}$  is the core surface flow,  $\nabla_H$  is the horizontal divergence operator and where we have neglected magnetic diffusion on the decadal and shorter timescales that are of interest here (see Finlay et al. (2016) for a discussion of the effects of diffusion on longer timescales).

Here, we present a quasi-geostrophic solution for  $\mathbf{u}$  obtained using the inversion method of Gillet et al. (2015b), taking as input the CHAOS-6 internal field to degree 13 and its SV to degree 16, evaluated at 1-year intervals between 1999.0 and 2016.0. We impose a columnar flow constraint at the core surface that follows from quasi-geostrophy and incompressibility in the outer core volume (Amit and Olson 2004)

$$\nabla_H \cdot (\mathbf{u} \cos^2 \theta) = 0, \quad (6)$$

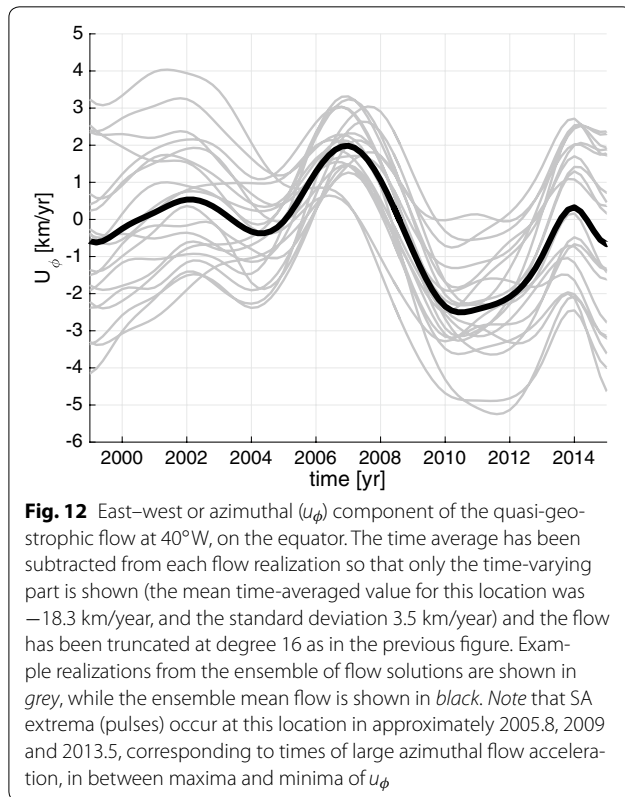
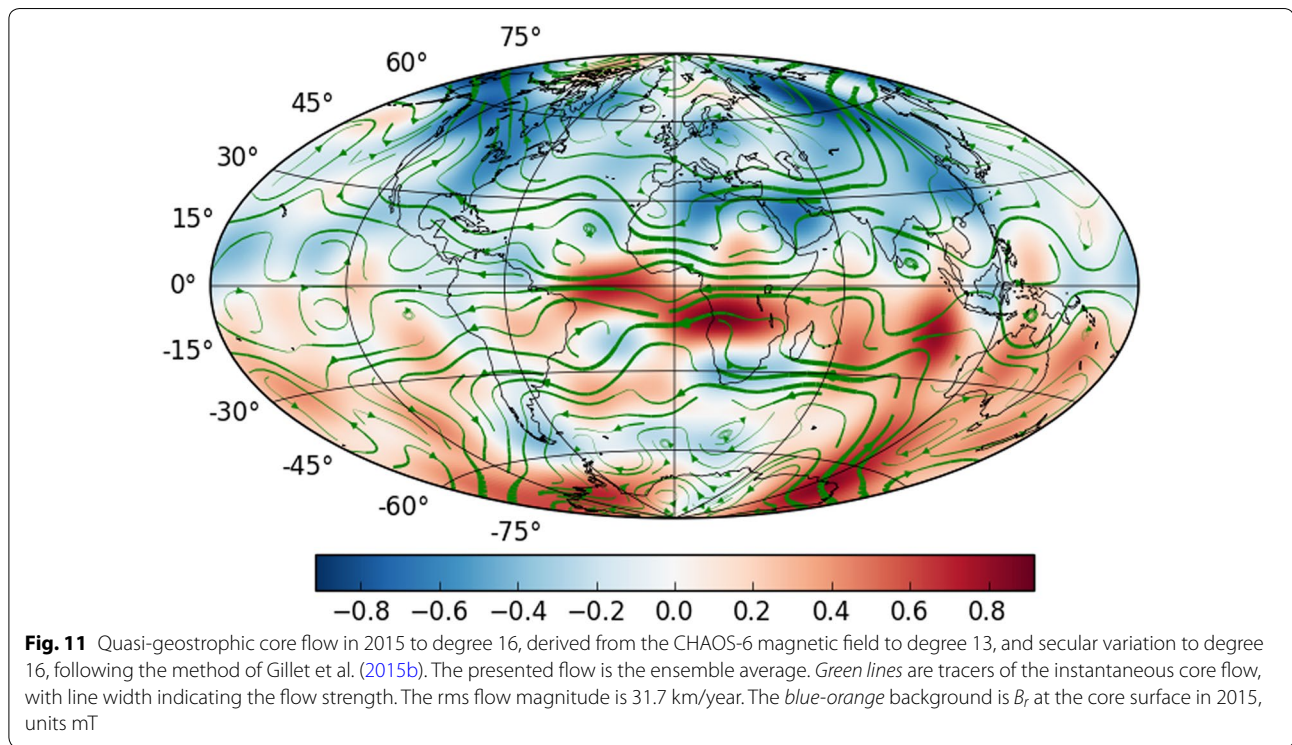
and also force the flow to be equatorially symmetric, consistent with core motions that are to leading order axially invariant (Pais and Jault 2008) so that,

$$u_\phi(\theta, \phi) = u_\phi(90 - \theta, \phi) \quad \text{and} \quad u_\theta(\theta, \phi) = -u_\theta(90 - \theta, \phi). \quad (7)$$

The core surface flow is expanded into toroidal and poloidal parts

$$\mathbf{u} = \nabla \times (T \mathbf{r}) + \nabla_H(rS), \quad (8)$$

where  $\mathbf{r}$  is the position vector and  $T$  and  $S$  are toroidal and poloidal scalars that are further expanded using a Schmidt semi-normalized spherical harmonic basis, up to degree and order 28. We consider in (5) temporally correlated SV model errors arising from the interaction of the flow with temporally correlated, but unresolved, small-scale field from degrees 14 to 30. An iterative scheme is employed, updating at each step the flow model covariance matrix using information from an ensemble of solutions. CHAOS-6 does not provide covariance information for the input SV, so we adopt simple diagonal covariances for the input SV, so we adopt simple diagonal covariances for the input SV observation errors. These are deduced from the errors provided by the COV-OBS.x1 field model (see Fig. 4 in Gillet et al. 2015a), with a fit to the SV uncertainties in 2010 extrapolated to degree 16. Further details of our flow inversion scheme may be



found in Gillet et al. (2015b). The flow models presented here go beyond those presented by Gillet et al. (2015b) in using SV to higher degree, and in focusing on explaining rapid field variations during the past 17 years when high-quality satellite data have been available.

A map of the resulting quasi-geostrophic flow in 2015, truncated at degree 16, is presented in Fig. 11. Here the green lines follow imaginary tracers in the flow, with the thickness of the line indicating the strength of the flow. At degree 16, the kinetic energy of the ensemble average flow is greater than 50 % of the kinetic energy of any of the ensemble realizations—see Gillet et al. (2015b), section 4.1 for a discussion of how the ensemble can be used to characterize the reliability of the inferred flow. As shown in Fig. 11, the flow is dominated by an anti-cyclonic, planetary-scale, eccentric gyre consisting of equatorward flow around 100°E, that then meanders westward flow in a belt around 20°–30°N and S of the equator, and then flows poleward again around 90°W, before closing with intense westward flow at high latitudes around 65°–75° N and S, close to the tangent cylinder that circumscribes the inner core. Broadly similar planetary gyres are found many recent flow inversions (e.g. Amit and Pais 2013; Aubert 2015; Gillet et al. 2015b; Baerenzung et al. 2016). The planetary gyre obtained here is, by construction, equatorially symmetric. Using

the high-resolution SV from CHAOS-6, we are able to obtain more detail regarding the small-scale structure of the gyre; the flow in Fig. 11 is presented to degree 16, while, for example, Gillet et al. (2015b) presented flows only to degree 14. We find the flow within the centre of the gyre is surprisingly quiescent, for example in the vicinity of the South Atlantic reverse flux patches. This is despite these lying in the Atlantic hemisphere, which is typically considered to be an active region characterized by high-amplitude SV.

In agreement with the findings of Gillet et al. (2015b), we find a series of prominent non-axisymmetric azimuthal (i.e. east–west, or  $u_\phi$ ) jets close to the equator. We find these jets undergo time-dependent oscillations at some locations, for example at 40°W at the equator—see Fig. 12. At this location, strong oscillations of the radial field SA are seen at the core surface. We find that pulses of SA at a particular location correspond to times of large acceleration in  $u_\phi$ , occurring between maxima and minima of  $u_\phi$ , for example at 40°W at the equator, where SA extrema occurred in 2005.8, 2009 and 2013.5.

Fig. 11 shows that azimuthal flows at low latitude are dominated by their non-axisymmetric part; their amplitude is significantly larger than that of the axisymmetric motions that are often interpreted as torsional Alfvén waves (Gillet et al. 2010, 2015b) in the same sub-decadal period range. Time–longitude plots of  $u_\phi$  at the equator do not show coherent propagation in longitude, but rather standing oscillatory features, with enhanced amplitude at particular locations. Interpretation of quasi-geostrophic flows at low latitudes requires pause for thought. Quasi-geostrophic models in a thin-shell ( $\beta$ -plane) geometry, as is relevant for the atmosphere and oceans, are known to break down at the equator. However, the outer core is a thick shell and recent tests of the quasi-geostrophic approximation in this geometry (comparing inertial modes in quasi-geostrophic models against full 3D solutions) show encouraging agreement, even for equatorially confined modes (Canet et al. 2014; Labbé et al. 2015). Further work is needed to better understand the dynamics of the low-latitude non-axisymmetric jets. For example: what drives such motions, and does the non-axisymmetric Lorentz force play an important role in producing the observed oscillations?

At this stage, it is important to recognize that other hypotheses are possible regarding the nature of the core flows. For example, there is presently a debate concerning whether a stratified layer may exist close to the core surface (e.g. Buffett 2014; Buffett et al. 2016; Chulliat et al. 2015; Lesur et al. 2015), inhomogeneous boundary conditions may force departures from equatorial symmetry (e.g. Amit and Pais 2013) or large scales may for some reason dominate the flow (e.g. Bloxham 1988;

Whaler and Beggan 2015). Nonetheless, the primary flow structures identified here, in particular equatorward flow in both the northern and southern hemispheres around 100°E and time-dependent non-axisymmetric westward flow at low latitudes, are sufficient to reproduce the observed rapid field changes, within the uncertainties due to the unresolved small-scale field.

## Conclusions

In this article, we have presented the CHAOS-6 field model and used it to analyse recent patterns of geomagnetic secular variation. CHAOS-6 includes more than 2 years of *Swarm* data and the latest ground observatory magnetic measurements as available in March 2016, along with data from previous satellite missions, and it provides information on geomagnetic secular variation between 1999.0 and 2016.5. It is the first member of the CHAOS field model series to use spatial field differences as data, utilizing along-track differences from both the *Swarm* and CHAMP satellites and east–west differences between *Swarm Alpha* and *Charlie*.

At Earth's surface, we find large-scale patterns of secular acceleration that change on short, sub-decadal, timescales. A geomagnetic jerk that occurred in 2014 is visible in Australia, and in the central Pacific, as well as in Europe. Transient accelerations are also seen in the strengthening and weakening of the field intensity; there has recently been a notable positive acceleration of the field intensity in the Asian longitude sector. CHAOS-6 captures the secular variation at the core surface up to at least spherical harmonic degree 16. Looking at the time derivative of this secular variation, the secular acceleration, we find that it has been dominated by a series of pulses, seen most clearly at low latitudes in the Atlantic sector and also at longitudes close to 100°E. Inverting the secular variation for a quasi-geostrophic core flow, we find the dominant time-averaged feature is a planetary-scale gyre structure that flows equatorward around 100°E, then westward at mid- to low latitudes and then poleward around 90°W, closing with intense westward flow at high latitudes close to the tangent cylinder. Rapid fluctuations are evident in the eastern, equatorward, limb of the gyre. In addition, the quasi-geostrophic flows show prominent oscillations of non-axisymmetric azimuthal jets at low latitudes that provide a possible explanation for localized, oscillatory SA pulses observed in this region, for example near to 40°W under northern South America.

Longer time series of *Swarm* data are needed to test and extend the preliminary results reported here for the secular variation and secular acceleration in 2015. The relatively long timescales involved, even for rapid secular acceleration pulses, mean that long-term monitoring

from space is essential if new hypotheses concerning the responsible core physics are to be properly tested. A lengthy *Swarm* mission, with the satellites gradually moving to lower altitudes, thus holds great promise. As the constellation configuration evolves, and the local time separation between the upper satellite and the lower pair increases, there will also be exciting opportunities to study secular variation on even shorter timescales.

The CHAOS-6 model is available from: [www.space-center.dk/files/magnetic-models/CHAOS-6](http://www.space-center.dk/files/magnetic-models/CHAOS-6).

#### Authors' contributions

CCF derived and analysed the CHAOS-6I model, drafted the manuscript and processed the ground observatory data to produce the revised monthly means and the RC index. NiO developed the CHAOS field modelling software, participated in the design of the study and derived and analysed the CHAOS-6h model. SK developed the scheme for using field differences in geomagnetic field modelling and participated in the design of the study. NG derived the quasi-geostrophic core flow models. LTC prepared and processed the *Swarm* data. All authors read and approved the final manuscript.

#### Author details

<sup>1</sup> Division of Geomagnetism, DTU Space, Technical University of Denmark, Diplomvej 371, Kongens Lyngby, Denmark. <sup>2</sup> ISTERre, Université Grenoble 1, CNRS 1381, rue de la Piscine, Grenoble Cedex 9, France.

#### Acknowledgements

We wish to thank ESA for providing access to the *Swarm* L1b data. The staff of the geomagnetic observatories and INTERMAGNET are thanked for supplying high-quality observatory data, and BGS are thanked for providing us with checked and corrected observatory hourly mean values. The support of the CHAMP mission by the German Aerospace Center (DLR) and the Federal Ministry of Education and Research is gratefully acknowledged. The Ørsted Project was made possible by extensive support from the Danish Government, NASA, ESA, CNES, DARA and the Thomas B. Thrives Foundation. CCF acknowledges support from the Research Council of Norway through the Petromaks programme, by ConocoPhillips and Lundin Norway and by the Technical University of Denmark. NG acknowledges support from French Agence Nationale de la Recherche (Grant ANR-2011-BS56-011) and the French Centre National d'Études Spatiales (CNES) for the study of Earth's core dynamics in the context of the *Swarm* mission of ESA, and ISTERre is part of Labex OSUG@2020 (ANR10 LABX56). Some numerical computations were performed at the Froggy platform of the CIMENT infrastructure (<https://ciment.ujf-grenoble.fr>) supported by the Rhône-Alpes region (GRANT CPER07\_13 CIRA), the OSUG@2020 labex (reference ANR10 LABX56) and the Equip@Meso project (reference ANR-10-EQPX-29-01). Nathanaël Schaeffer is thanked for assistance in producing the core flow map, Fig. 11. Two anonymous reviewers are thanked for their comments that helped to improve the clarity of the manuscript.

#### Competing interests

The authors declare that they have no competing interests.

Received: 31 December 2015 Accepted: 9 June 2016

Published online: 11 July 2016

#### References

- Amit H, Olson P (2004) Helical core flow from geomagnetic secular variation. *Phys Earth Planet Int* 147(1):1–25
- Amit H, Pais MA (2013) Differences between tangential geostrophy and columnar flow. *Geophys J Int* 194:145–157
- Aubert J (2015) Geomagnetic forecasts driven by Earth's core thermal wind dynamics. *Geophys J Int* 203:1738–1751
- Baerenzung J, Holschneider M, Lesur V (2016) The flow at the Earth's core–mantle boundary under weak prior constraints. *J Geophys Res Solid Earth* 121(3):1343–1364. doi:10.1002/2015JB012464
- Bloxham J (1988) The determination of fluid flow at the core surface from geomagnetic observations. In: Vlaar NJ, Nolet G, Wortel MJR, Cloetingh SAPL (eds) *Mathematical geophysics, a survey of recent developments in seismology and geodynamics*. Reidel, Dordrecht, pp 189–208
- Buffett BA (2014) Geomagnetic fluctuations reveal stable stratification at the top of the Earth's core. *Nature* 507:484–487
- Buffett BA, Knezek N, Holme R (2016) Evidence for MAC waves at the top of Earth's core and implications for variations in length of day. *Geophys J Int* 204:1789–1800
- Canet E, Finlay CC, Fournier A (2014) Hydromagnetic quasi-geostrophic modes in rapidly rotating planetary cores. *Phys Earth Planet Int* 229:1–15
- Chulliat A, Maus S (2014) Geomagnetic secular acceleration, jerks, and a localized standing wave at the core surface from 2000 to 2010. *J Geophys Res*. doi:10.1002/2013JB010604
- Chulliat A, Thébault E, Hulot G (2010) Core field acceleration pulse as a common cause of the 2003 and 2007 geomagnetic jerks. *Geophys Res Lett*. doi:10.1029/2009GL042,019
- Chulliat A, Alken P, Maus S (2015) Fast equatorial waves propagating at the top of the Earth's core. *Geophys Res Lett* 42:3321–3329
- Clarke E, Baillie O, Reay S (2013) A method for the real time production of quasi-definitive magnetic observatory data. *Earth Planets Space* 65:1363–1374
- De Boor C (2001) *A practical guide to splines*. Springer-Verlag, New York
- Finlay CC, Olsen N, Tøffner-Clausen L (2015) DTU candidate field models for IGRF-12 and the CHAOS-5 geomagnetic field model. *Earth Planets Space*. doi:10.1186/s40623-015-0274-3
- Finlay CC, Aubert J, Gillet N (2016) Gyre-driven decay of the earth's magnetic dipole. *Nat Commun* 7(10):422. doi:10.1038/ncomms10422
- Gellibrand H (1635) A discourse mathematical on the variation of the magnetic needle. Together with its admirable diminution lately discovered. William Jones, London
- Gillet N, Jault D, Canet E, Fournier A (2010) Fast torsional waves and strong magnetic field within the Earth's core. *Nature* 465:74–77. doi:10.1038/nature09010
- Gillet N, Jault D, Finlay CC, Olsen N (2013) Stochastic modeling of the Earth's magnetic field: inversion for covariances over the observatory era. *Geochim Geophys Geosyst*. doi:10.1029/2012GC004355
- Gillet N, Barrois O, Finlay CC (2015a) Stochastic forecasting of the geomagnetic field from the COV-OBSx.1 geomagnetic field model, and candidate models for IGRF-12. *Earth Planets Space*. doi:10.1186/s40623-015-0225-z
- Gillet N, Jault D, Finlay CC (2015b) Planetary gyre and time-dependent midlatitude eddies at the Earth's core surface. *J Geophys Res* 120:3991–4013
- Hansteen C (1819) *Untersuchungen über den Magnetismus der Erde*. Lehmann and Gröndahl, Christiania
- Holme R, Bloxham J (1996) The treatment of attitude errors in satellite geomagnetic data. *Phys Earth Planet Int* 98:221–233
- Holme R, Olsen N, Bairstow F (2011) Mapping geomagnetic secular variation at the core–mantle boundary. *Geophys J Int* 186:521–528. doi:10.1111/j.1365-246X.2011.05066.x
- Jackson A, Jonkers ART, Walker MR (2000) Four centuries of geomagnetic secular variation from historical records. *Philos Trans R Soc Lond A* 358:957–990
- Kotsiaros S, Finlay CC, Olsen N (2014) Use of along-track magnetic field differences in lithospheric field modelling. *Geophys J Int* 200:878–887
- Labbé F, Jault D, Gillet N (2015) On magnetostrophic inertia-less waves in quasi-geostrophic models of planetary cores. *Geophys Astrophys Fluid Dyn* 109:587–610
- Langel RA, Mead GD, Lancaster ER, Estes RH, Fabiano EB (1980) Initial geomagnetic field model from Magsat vector data. *Geophys Res Lett* 7:793–796
- Lesur V, Wardinski I, Rother M, Manda M (2008) GRIMM: the GFZ reference internal magnetic model based on vector satellite and observatory data. *Geophys J Int* 173:382–394
- Lesur V, Wardinski I, Hamoudi M, Rother M (2010) The second generation of the GFZ reference internal magnetic model: GRIMM-2. *Earth Planets Space* 62:765–773. doi:10.5047/eps.2010.07.007
- Lesur V, Whaler K, Wardinski I (2015) Are geomagnetic data consistent with stably stratified flow at the core–mantle boundary? *Geophys J Int* 201:929–946
- Lesur V, Rother M, Wardinski I, Schachtschneider R, Hamoudi M, Chambodut A (2015) Parent magnetic field models for the IGRF-12 GFZ-candidates. *Earth Planets Space* 67:87. doi:10.1186/s40623-015-0239-6

- Macmillan S, Olsen N (2013) Observatory data and the Swarm mission. *Earth Planets Space* 65:1355–1362
- Maus S (2010) Magnetic field model MF7. [www.geomag.us/models/MF7.html](http://www.geomag.us/models/MF7.html)
- Olsen N, Lühr H, Sabaka TJ, Manda M, Rother M, Tøffner-Clausen L, Choi S (2006) CHAOS—a model of Earth's magnetic field derived from CHAMP, Ørsted, and SAC-C magnetic satellite data. *Geophys J Int* 166:67–75
- Olsen N, Manda M, Sabaka TJ, Tøffner-Clausen L (2009) CHAOS-2—a geomagnetic field model derived from one decade of continuous satellite data. *Geophys J Int* 179(3):1477–1487
- Olsen N, Manda M, Sabaka TJ, Tøffner-Clausen L (2010) The CHAOS-3 geomagnetic field model and candidates for the 11th generation of IGRF. *Earth Planets Space* 62:719–727
- Olsen N, Lühr H, Finlay CC, Tøffner-Clausen L (2014) The CHAOS-4 geomagnetic field model. *Geophys J Int* 197:815–827
- Olsen N et al (2015) The Swarm initial field model for the 2014 geomagnetic field. *Geophys Res Lett* 42:1092–1098
- Olsen N, Finlay CC, Kotsiaros S, Tøffner Clausen L (2016) A model of Earth's magnetic field derived from two years of Swarm data. *Earth Planets Space*. doi:10.1186/s40623-016-0488-z
- Pais MA, Jault D (2008) Quasi-geostrophic flows responsible for the secular variation of the Earth's magnetic field. *Geophys J Int* 173:421–443
- Peltier A, Chulliat A (2010) On the feasibility of promptly producing quasi-definitive magnetic observatory data. *Earth Planets Space* 62:e5–e8. doi:10.5047/eps.2010.02.002
- Richmond AD (1995) Ionospheric electrodynamics using magnetic Apex coordinates. *J Geomagn Geoelectr* 47:191–212
- Sabaka TJ, Olsen N, Purucker ME (2004) Extending comprehensive models of the Earth's magnetic field with Ørsted and CHAMP data. *Geophys J Int* 159:521–547
- Sabaka TJ, Olsen N, Tyler R, Kuvshinov A (2015) CM5, a pre-Swarm comprehensive magnetic field model derived from over 12 years of CHAMP, Ørsted, SAC-C and observatory data. *Geophys J Int* 200:1596–1626. doi:10.1093/gji/ggu493
- Shure L, Parker RL, Backus GE (1982) Harmonic splines for geomagnetic modeling. *Phys Earth Planet Int* 28:215–229. doi:10.1016/0031-9201(82)90003-6
- Tøffner-Clausen L, Lesur V, Brauer P, Olsen N, Finlay CC (2016) In-flight scalar calibration and characterisation of the swarm magnetometry package. *Earth Planets Space* 200 (in press)
- Torta JM, Pavón-Carrasco FJ, Marsal S, Finlay CC (2015) Evidence for a new geomagnetic jerk in 2014. *Geophys Res Lett* 42(19):7933–7940. doi:10.102/2015GL065501
- Whaler KA, Beggan CD (2015) Derivation and use of core surface flows for forecasting secular variation. *J Geophys Res* 120:1400–1414

Submit your manuscript to a SpringerOpen® journal and benefit from:

- Convenient online submission
- Rigorous peer review
- Immediate publication on acceptance
- Open access: articles freely available online
- High visibility within the field
- Retaining the copyright to your article

---

Submit your next manuscript at ► [springeropen.com](http://springeropen.com)

---